

Integrated nano electro-optomechanical spiking neuron

Gregorio Beltramo¹, Róbert Horváth¹, Grégoire Beaudoin¹,
Isabelle Sagnes¹, Sylvain Barbay¹, Rémy Braive^{1,2,3*}

¹Centre de Nanosciences et Nanotechnologies, Université Paris Saclay,
Palaiseau, 91120, France.

²Université Paris Cité, Paris, 75006, France.

³ Institut Universitaire de France, Paris, 75231, France.

*Corresponding author(s). E-mail(s): remy.braive@c2n.upsaclay.fr;

Abstract

Neuromorphic computing offers a pathway toward energy-efficient processing of data, yet hardware platforms combining nanoscale integration and multimodal functionality remain scarce. Here we demonstrate a gallium-phosphide electro-optomechanical spiking neuron that integrates optical and electromechanical interfaces within a single nanostructure on a silicon photonic chip operating at telecommunication wavelengths (1550 nm) and exploiting a 3 gigahertz-frequency mechanical mode. Our device displays excitable dynamics, generating optical spikes at its output, as in the spiking activity of neurons and cardiac cells and defined by the calibrated all-or-none response to external perturbations. This dynamic is consistent with the saddle-node on invariant circle scenario and associated features are demonstrated including control of excitable threshold, temporal summation and refractory period. Our device compact footprint and its CMOS-compatible platform make it well suited for edge-computing applications requiring low latency and establish a foundation for versatile brain-inspired optomechanical computing and advanced on-chip optical pulse sources.

Among the numerous possibilities for building artificial neural networks hardware [1], those based on biologically inspired spiking neurons form the third generation of neural networks [2]. Neuromorphic computers can perform computation through directed graphs that are better suited for the collocation of computing units and memory much like the human brain. Each neuron is an individual computing unit with its own dedicated memory such that multiple pieces of information can be processed completely asynchronously and in parallel [3]. Within this framework, spiking or excitable neurons act as a building blocks for brain-inspired, neuromorphic computing architectures, offering new ways to represent information that may be more natural for specific classes of computation, such as graph algorithms [4], quadratic programming [5], and other parallelizable computation algorithms [6]. Encoding of information in the form of spike timing (temporal coding) or the spike rate (rate coding) has been investigated and subject to active research [7, 8]. Excitable neurons are also attracting increasing interest because of their ability to compute a task using minimal resources, hence enabling potentially less energy consumption [9, 10].

A hallmark of an excitable behaviour is the calibrated, all-or-none response to a perturbation. An excitable system possesses one stable state. When subject to a perturbation, the system remains in its quiet, stable state if the perturbation amplitude is smaller than a certain threshold. If the perturbation amplitude exceeds this threshold (the excitable threshold), the system performs a characteristic excursion in phase space generally associated to the generation of a pulse and returns to its stable state. Excitability has been demonstrated in many physical systems, including memristors [11], spintronic oscillators [12], Josephson junctions [13], microfluidics [14] and lasers or optical systems [15–21]. One of the possible underlying physical mechanisms corresponds to a Saddle Node on Invariant Circle (SNIC) bifurcation [22]. From a nonlinear dynamical point of view, the phase dynamics of a nonlinear oscillator can be generically represented by an invariant circle encircling the origin in phase space. In

the unlocked regime, the oscillator phase rotates freely on the circle. However, in the injection-locked regime, the system's phase settles to a fixed stable point that appears on the circle together with an unstable fixed point, following a saddle-node bifurcation. When perturbed beyond the minimum distance between these two fixed points, the system follows a deterministic and repeatable trajectory in phase space to return to its stable state after completing a full 2π phase excursion. Usually associated to a spike in the amplitude response, this specific property can be found in injected single-mode oscillators, near the locked - unlocked transition and characterizes the excitable behaviour.

Optoelectronic implementations of artificial spiking neural networks have been developed to combine the advantage of well-studied electronic nonlinearities alongside the fast, lossless transmission and zero-energy weighting provided by the photonic devices [23–26]. However, such a neuron architecture necessitates the use of electronic/optical conversions hence a potential loss of speed, increased complexity and thus increased energy consumption. Despite the integration of CMOS transistors with photodiodes and electro-optic modulators, the response speed of a single optoelectronic neuron is limited because of the analogue bandwidth of the electronics, unlike all-optical neurons. More recently, Micro/Nano Electro-Mechanical Systems (MEMS/NEMS) have been considered for classical echo-state (non-spiking) reservoir computing [27–29] and for image classification using the nonlinear transfer function of the mechanical response [30]. At last, a MHz thermo-optomechanical neuron-like behaviour has been reported in a silicon microcavity [31]. Due to the coexistence on the same device of photonic and mechanical degrees of freedom, optomechanical resonators [32] have the advantage of their all-optical counterpart and of naturally generating a radio-frequency (RF) signal like in Opto-electronic Oscillators (OEO). Besides quantum technologies developments [33], they present an extraordinary and yet scarcely explored platform for neuromorphic architectures incorporating spiking artificial neurons.

We demonstrate here the excitable behavior of a self-sustained, 3.1 GHz electro-optomechanical oscillator (E-OMO) made of Gallium Phosphide (GaP) and integrated on a Silicon-on-Insulator (SoI) photonic chip working at 1550 nm. Thanks to the piezoelectricity of GaP, injection locking of the electro-optomechanical oscillator to an external RF driving signal is achieved through on-chip integrated electrodes. External optical perturbations at the optical input port allow to reveal the excitable response. A statistical analysis is performed as a function of the perturbation strength as well as the RF drive detuning. Calibrated all-or-none responses are experimentally evidenced thus demonstrating the excitable behavior of the E-OMO. Beyond excitability, other neuromorphic features such as temporal summation and refractory periods are observed which pave the way to a novel integrated, analog neuromorphic computing platform.

1 Electromechanical injection locking

We first discuss the electromechanical injection locking of our E-OMO. Our device consists of a 300 nm-thick gallium phosphide (GaP) and free-standing 1D optomechanical crystal (in blue in figure 1a) heterogeneously integrated on top of a SoI circuitry (See Methods for more details). The control of the position of the holes along the 1D optomechanical crystal structure allows to simultaneously confine photons around 1550 nm and phonons close to 3.1 GHz, giving rise to a large optomechanical coupling constant. The optomechanical crystal is optically addressed through an underneath SoI optical waveguide (in red in figure 1a). A tunable laser, coupled to the SoI waveguide thanks to a grating coupler, is put on resonance with the optical mode of the 1D nanobeam at 1550.5 nm. Light is then coupled out through another grating coupler to be analyzed. At low input optical power P_{in} (measured before the input to the grating coupler), a fine scanning of the input wavelength gives access to a high resolution transmission spectrum as measured with a power meter (PM in fig. 1b) and

hence to the total optical quality factor (Q_o) of about 44×10^3 . For $P_{in} = 80 \mu\text{W}$, and at $\lambda_o = 1550.5 \text{ nm}$, output light is characterized by a fast photo-diode and analyzed with an electrical spectrum analyzer (ESA - Fig. 1b). The mechanical response of the optomechanical crystal is assessed under atmospheric conditions, allowing one to extract the mechanical resonant frequency $\Omega_m/2\pi = 3.078 \text{ GHz}$, the mechanical quality factor $Q_m \approx 1550$ and the optomechanical coupling constant $g_0/2\pi = 600 \text{ kHz}$. By increasing input optical power P_{in} , self-sustained optomechanical oscillations [34] appear above a given threshold and are evidenced by the sharp increase of the amplitude of the investigated mechanical mode (Fig. 1e). A non-linear frequency shift with optical power is also clearly visible because of the competition between optical spring effect and thermo-mechanical shift [35]. Nevertheless, the positive shift suggests that the former is the main factor at play here. The two frequency sidebands visible in the mechanical RF spectrum are related to the mixing of the self-oscillating mode with a low frequency mechanical mode at 2 MHz. In the following, we set the injected optical power at $P_{in} = P_b \equiv 1.51 \text{ mW}$.

Electromechanical control of the mechanical mode [34, 36] is obtained thanks to the piezoelectric properties of GaP, using 1 μm wide metallic electrodes (in yellow in figure 1a) located near the center of the nanobeam cavity. A lock-in amplifier is used to inject a RF drive at a fixed peak-to-peak voltage $V_{RF} = 100 \text{ mV}$. By sweeping its frequency f_d upwards in the vicinity of the mechanical resonance $\Omega_m/2\pi$, different responses are visible on the ESA (Fig. 1d). For f_d away from $\Omega_m/2\pi$, two peaks appear on the spectrum: the sharp one corresponds to the RF drive whereas the larger one is the mechanical mode distorted by the presence of the drive. Note that depending on the sign of the detuning $\Omega_d - \Omega_m$, the large spectral feature displays a distortion in opposite directions, due to the nonlinear frequency mixing between the self-induced optomechanical oscillation and the RF drive. By contrast, when the drive is closer to the natural frequency of the mechanical self-oscillator $\Omega_m/2\pi$, only a

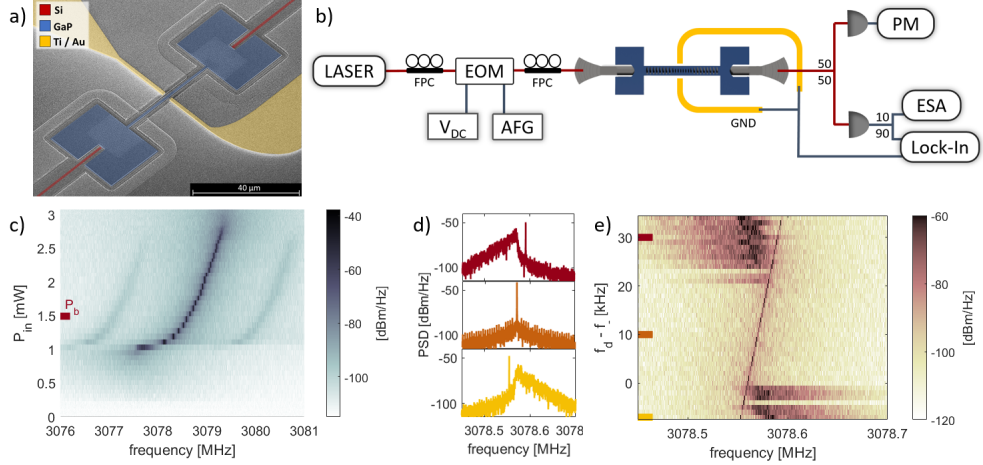


Figure 1 a) Colored SEM image of the electro-optomechanical oscillator showing the piezoelectric Gallium Phosphide photonic crystal nanobeam cavity (in blue) suspended on top of a silicon-on-insulator bus waveguide (in red) and with gold electrodes (in yellow) positioned on both sides of the PhC nanobeam cavity. b) Experimental setup: tunable fibered IR laser (LASER), fibered polarization controller (FPC), 10 GHz bandwidth electro-optic modulator (EOM), bias voltage supply (V_{DC}) and arbitrary function generator (AFG) constitute the excitation scheme. After the electro-optomechanical oscillator, the optical signal is split in two ports (50/50) and directed to an optical powermeter (PM) and a fast, 3.5 GHz bandwidth, photo-detector. The photodetected electrical signal is split 90% to the lock-in amplifier and 10% to the electric spectrum analyzer (ESA). The digital lock-in amplifier generates the RF driving at frequency f_d at the gold electrodes. c) Power spectral density map of the photodetected signal recorded at the ESA as a function of the input power P_{in} . The highlighted power level $P_{in} = P_b = 1.51$ mW corresponds to the one used for excitability measurements. d) Power spectral densities for $P_{in} = P_b$ and for three distinct frequency offsets $f_d - f_- = -7, 10, 30$ kHz: before (bottom - yellow), inside (middle - orange) and after (top - red) the locking region, respectively. In c-d), $V_{RF} = 100$ mV. e) Full power spectral density map of the photodetected signal as a function of the driving frequency offset for the same parameters as in c-d).

single peak is present (middle panel in figure 1d). This evidences injection locking of the mechanical mode with the external RF drive. By recording responses over a larger frequency range, the full electro-mechanical injection locking region can be observed with a width of 23 kHz (Fig. 1e) for the specific parameters chosen here ($V_{RF} = 100$ mV and $P_b = 1.51$ mW). The low and high frequency edges of the locking region are named f_- and f_+ respectively in the following.

2 Excitability of the Electro-optomechanical oscillator

In order to study the excitability of the E-OMO, the RF detuning is set inside the locking region in the vicinity of its low-frequency edge ($f_d - f_- = 6$ kHz) while the wavelength of the optical input is kept at $\lambda_o = 1550.5$ nm. Optical perturbations are imprinted onto the input optical field thanks to a Lithium-Niobate electro-optic modulator (EOM in figure 1b) controlled by an arbitrary function generator (AFG in figure 1b) and a DC electric bias. The optical perturbations (P_{pulse}) are set as a pulse train of rectangular pulses having 1 μ s duration with a duty cycle of 0.5 %, sitting on-top of a DC optical bias (P_b) such that $P_{in}(t) = P_b + P_{pulse}$. The time trace of the perturbations is illustrated in figure 2a for two periods. The optical response of the system is displayed in Figure 2b-d for three different values of the perturbation pulse P_{pulse} , namely 10%, 45% and 80% of P_b respectively. The time elapsed since the perturbation is color-coded with a logarithmic scale from 0 (yellow) to 200 μ s (dark blue). Moreover, the corresponding phase portrait of the transmitted optical signal (with quadratures $I(t)$ and $Q(t)$) are shown as insets where the colors are consistent with the time traces. The gray dotted circle is a guide for the eyes, highlighting the phase space that the system would explore if unlocked to the external RF driving and with no amplitude dynamics (pure phase oscillator case).

The mechanism leading to phase perturbations can be understood by looking at figure 1c. An increase of the input intensity P_{in} induces a shift of the oscillation frequency. Thus, the optical power perturbations cause abrupt and intermittent phase kicks to the system. As the amplitude of the perturbation increases, the phase shift gets larger till a point where it can exceeds a phase threshold ϕ_{th} (see Figs. 2b-d). In the case of a weak perturbation ($0.1 \times P_b$, Fig. 2b), practically no amplitude response is visible and the E-OMO remains locked as can be seen in the phase space representation, where the system stays close to the stable locked phase. Small deviations

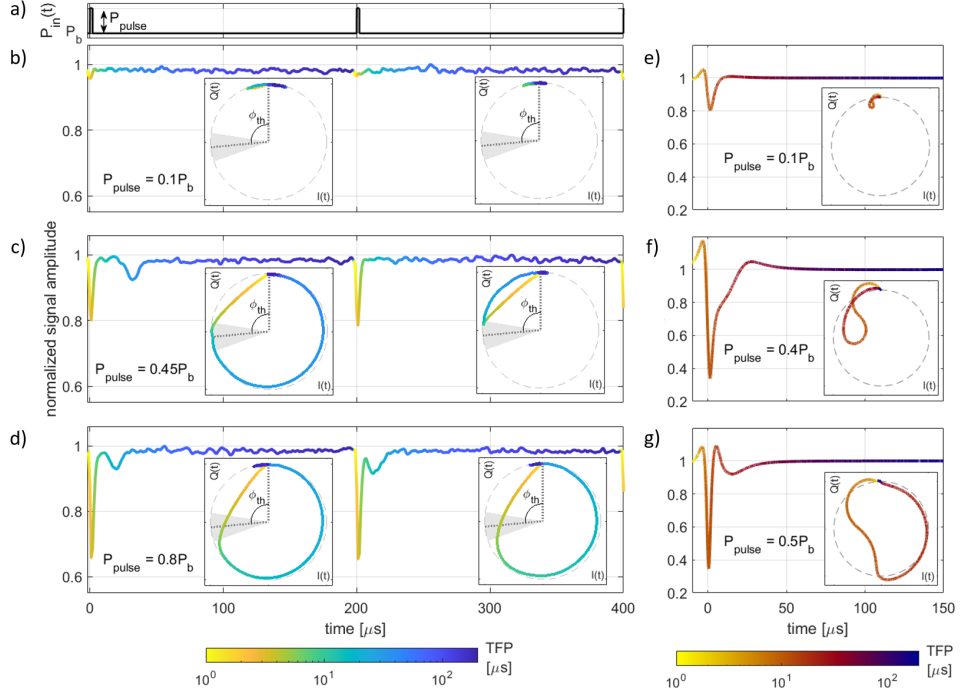


Figure 2 Spiking responses of electro-optomechanical oscillator subject to a perturbation. a) Temporal evolution of the optical input power sent to the device consisting of a bias, cw excitation $P_b = 1.51$ mW, plus a pulse train of rectangular perturbations with $1\ \mu\text{s}$ wide pulses of amplitude P_{pulse} and $200\ \mu\text{s}$ period. b-d) Normalized time evolution of the output signal amplitude recorded by the digital lock-in amplifier after demodulation for P_{pulse} equals to (b) $0.1 \times$, (c) $0.45 \times$ and (d) $0.8 \times P_b$. The time from perturbation (TFP) is color-coded with a logarithmic scale from the perturbation pulse arrival (in yellow) to $200\ \mu\text{s}$ after the perturbation (in dark blue). e-g) Numerical simulations of the normalized signal amplitude response after numerical demodulation for P_{pulse} equals to (e) $0.1 \times$, (f) $0.4 \times$ and (g) $0.5 \times P_b$ with the time evolution color-coded in the same way as in the experiment. In insets: phase space reconstructed from the demodulated quadratures $I(t)$ and $Q(t)$. The gray dotted circle represents the phase space dynamics of a pure phase oscillator in the unlocked regime. The dashed black lines in the experimental phase space diagram mark the average estimated positions of the stable and unstable phase equilibria and their difference ϕ_{th} , for the specific experimental conditions.

from the stable locked phase are nevertheless evidenced because of environmental and experimental noises. Note also that an upward perturbation pulse in the input optical power translates here into a dip in the optical response envelope dynamics. For a slightly larger amplitude perturbation strength ($0.45 \times P_b$, Fig. 2c), close to the locked-unlocked perturbation threshold ϕ_{th} , the first perturbation induces a response a few tenths of microseconds later, evidenced by the presence of a downward peak in the

signal amplitude, unlike the second one. From the inspection of the phase space, we observe that the first perturbation is strong enough to unlock the system and induce a 2π , counter clock-wise phase excursion so that the system returns to its original stable locked state (left inset). By contrast, the second perturbation does not produce a full 2π phase excursion (right inset). Rather, the system settles back to the stable locked phase in the clockwise direction without any noticeable amplitude response. For an even stronger perturbation amplitude ($0.8 \times P_b$, Fig. 2d), each perturbation is sufficient to excite a response pulse as evidenced by the presence of downward peaks following both perturbations. In the two phase space representations (see insets), it can be noticed that the perturbations are strong enough to induce a 2π phase excursion before the system settles back to its original locked state. This behavior is very typical of an excitable response in a SNIC scenario[22]. There exists a clear threshold in the optical perturbation amplitude which produces a full 2π phase excursion in the response. Besides the 2π phase excursion, the response is associated with an amplitude response (a small downward pulse) since our E-OMO is not a pure phase oscillator but possesses an amplitude dynamics too. Close to the excitable threshold (Fig. 2c), noise can trigger or not a response. However, the response is always of the all-or-none type, since the phase excursion is either a full 2π excursion or a return back to the original locked phase, and the amplitude response is either a calibrated downward pulse or practically none. For perturbations well above the threshold (Fig. 2d), the response is always present and remains calibrated in phase or in amplitude. In the phase space representation, the transition from clockwise return to locked phase and full 2π counter-clockwise phase excursion reveals the presence of an unstable fixed point, which is marked by a dashed line in the experimental phase-space representations associated to a gray segment that represents the calculated experimental uncertainty in its position, obtained from the time evolutions of the recorded phase (not shown here). In particular this allows to reconstruct the relative phase difference

between the stable and unstable fixed points, which are represented by the angle ϕ_{th} in every experimental insets.

Numerical simulations of the optically perturbed E-OMO are carried out with parameters extracted from the experiment (see Methods for details on the modelling and numerical simulations) and their results are displayed in Figure 2 e–g. The plotted signal is numerically demodulated in the same way as in the experiment to allow for direct comparison. Figure 2 e–g shows the time evolution of the normalized signal amplitude for three distinct perturbation amplitudes P_{pulse} . For a small perturbation amplitude ($P_{\text{pulse}} = 0.1 \times P_b$ - Fig. 2e), which appears similarly as in the experiment as a downward signal, the E-OMO is not perturbed strong enough to induce a full 2π phase excursion. Rather, a small dynamics near the stable locked phase is visible in phase-space, as a consequence of the small input perturbation. Note that the simulations are performed without added noise, and are thus purely deterministic. For an intermediate perturbation amplitude ($P_{\text{pulse}} = 0.4 \times P_b$ - Fig. 2f), close but below the excitable threshold, an asymmetric response is visible without a complete excursion in phase space. For an even larger perturbation ($P_{\text{pulse}} = 0.5 \times P_b$ - Fig. 2g), two distinct downward pulses separated by about $15\mu\text{s}$ appear. In the phase space representation and with the color-coding of the time from perturbation, it appears that the second pulse is associated with the 2π phase excursion, evidencing the numerical excitable response. The good qualitative agreement with the experimental recordings validates the model used here, and confirms the excitable response experimentally observed. The only difference here is that no noise has been injected in the numerical simulations, therefore no noise excited excitable pulse can be observed.

3 Characterization of excitable response main properties

The excitable threshold as well as the time delay between the perturbation and the excitable response (spike latency) are characterized by perturbing 5000 times (overall time traces of 1 second) the locked state with the same parameters ($P_b = 1.51$ mW and $f_d - f_- = 6$ kHz) and performing a statistical analysis of the response. Fig. 3a shows the median of the absolute value of the response amplitude to a single perturbation with 30-70 percentiles. For low perturbation powers until $P_{\text{pulse}} \simeq 0.35 \times P_b$, the median of the response amplitude is 0 since the perturbation never or rarely gives rise to an excitable response. Above this threshold ($P_{\text{pulse}} \gtrsim 0.4 \times P_b$), excitable pulses appear with a calibrated amplitude response median, a sign of the calibrated excitable response pulse whose amplitude hardly depends on the perturbation strength. This is a clear signature of the expected all-or-none response, with a marked threshold. Fig. 3b displays the spike latency as a function of the perturbation amplitude P_{pulse} . It shows a highly nonlinear evolution, with low latencies associated to high perturbation amplitudes followed by a rapidly increasing latency around the excitable threshold till a zero latency corresponding to no emitted pulse at all. It could be found at least curious or even wrong that latency times could be extracted below the excitable threshold, in the grayed region in fig. 3b). However, this is easily understood when considering the noise in the system. Indeed, for non-zero perturbation amplitude P_{pulse} but below the excitable threshold (in the gray area), a median for the spike latency can still be extracted because of frequent noise-induced pulses, until a point where the noise is no more strong enough to induce noise-excited excitable responses. The overall latency is well inline with what is expected in the excitable regime, with a divergence of the latency time at the excitable threshold in the deterministic case. A reduction in latency by a factor 4 is evidenced when the perturbation amplitude increases by a factor about 20, where the spike latency reaches saturation at $15 \mu\text{s}$ above $0.75 \times P_{in}$. This

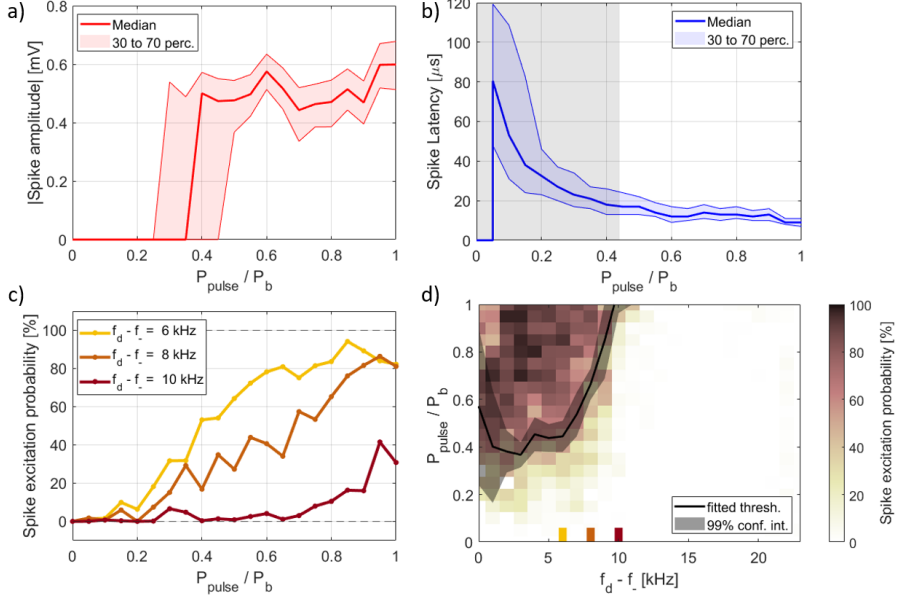


Figure 3 Statistical analysis of the excitable response as a function of the perturbation amplitude. a) Median amplitude of the spiking response in absolute value, at $f_d - f_- = 6$ kHz. The shaded region refers to the 30th and 70th percentiles. b) Median spike latency, at $f_d - f_- = 6$ kHz. The shaded blue region refers to the 30th and 70th percentiles whereas the gray shaded one refers to the below-threshold perturbation amplitudes, $P_{pulse} \gtrsim 0.44 \times P_b$. c) Spike excitation probability as a function of the perturbation amplitude for three different values of $f_d - f_-$: 6 kHz (yellow), 8 kHz (orange) and 10 kHz (dark red). d) Map of the spike excitation probability (color-scale) as a function of the perturbation amplitude and of the RF drive detuning $f_d - f_-$.

saturation value is of the same order as the one reached in the numerical simulations, as can be observed in Fig. 2g. Note that spike latency introduces an important brain-inspired computing mechanism for encoding input perturbations in the time domain of the output spikes [7, 8].

The probability of triggering an excitable pulse is investigated as a function of the optical perturbation amplitude for different RF drive detunings in Fig. 3c. For $f_d - f_- = 6$ kHz, the probability reaches over 80 % beyond a perturbation amplitude of $0.75 \times P_b$ (Fig. 3c - yellow curve). By going deeper in the locking region, stronger perturbations are needed to reach efficient excitability (above 100% P_b for $f_d - f_- = 8$ kHz - orange curve in fig. 3c), up to a frequency detuning of 10 kHz (red curve in fig. 3c) where no more than 40 % efficiency can be reached within the linearity range

of the EOM. The probability for an excitable pulse response is fully mapped in the plane of the detuning of the RF drive versus the amplitude of the optical perturbation P_{pulse} (figure 1d). For each detuning, the evolution as a function of the power ratio is fitted with a sigmoid function. The 50 % limit is highlighted in black, and the 99 % confidence interval is highlighted in shaded gray. Close to the locking-unlocking transition, below 2 kHz, a reduced switching efficiency is observed due to an averaging effect of the noise-induced fluctuations of the mechanical self-oscillation frequency. At 2 kHz detuning, the 50 % limit is reached around $P_{\text{pulse}} = 0.4 \times P_b$ and the probability of over 90 % is achieved with a pulse power of $0.7 \times P_b$. By further increasing the detuning, the 50 % limit is slightly reduced till 6 kHz. Beyond this detuning, the strength of the perturbation amplitude required to reach 50 % rapidly increases and the excitable efficiency drops. Beyond 10 kHz, the observation of excitability is no longer possible with the current experimental apparatus and available perturbation amplitudes. However, we expect a strong increase of the perturbation amplitude in this regime and even the disappearance of the excitable response. This shift to higher perturbation amplitudes as the detuning of the RF drive gets larger demonstrates the possibility to easily tune and control the excitable threshold. Indeed, keeping P_b fixed while increasing the detuning ($f_d - f_-$) increases the excitable threshold, making excitable pulses harder to excite. This simple behaviour is important in the context of analog brain inspired computing, as e.g. demonstrated in a photonic context in [37].

4 Summation and Refractory periods

Beyond the excitable response, biological neurons show other important features such as temporal summation and refractory periods. The ability of neurons to integrate sub-threshold input signals received on their input channels can be probed by studying the dynamical response to consecutive below-threshold perturbations depending on their separation in time [38]. Two equal and below-threshold optical perturbation

pulses ($P_{pulse} = 0.4 \times P_b$ and $1 \mu s$ pulse width) with a controllable time delay Δt are prepared. For a time delay $\Delta t = 13 \mu s$, figure 4a shows the normalized signal amplitude in time while the corresponding phase space is displayed in Fig. 4b. It is clear from the two plots that the two consecutive perturbations do not induce an excitable response. However, by reducing the time delay down to $\Delta t = 7 \mu s$, the two perturbations can add up so that an excitable response can be observed in the normalized signal amplitude (fig. 4d) after the second perturbation. The corresponding phase space (fig. 4e) highlights the 2π phase shift evidencing the excitable behavior for two sub-threshold perturbations. This behaviour is well reproduced in the numerical simulations of our model in 2e–g, where two successive square wave optical power perturbations are introduced as inputs into the cavity. For below threshold perturbations ($P_{pulse} = 0.3 \times P_b$ and $f_d - f_- = 15 \text{ kHz}$), simulated phase spaces for $\Delta t = 6 \mu s$ and $4 \mu s$ are shown in figure 4c and f respectively. In the first case (Fig. 4c) the pulses are too far away apart to trigger an excitable response and a 2π phase excursion. In the second case, (Fig. 4d), a 2π phase excursion is produced.

Another important feature of neurons concerns the response to successive, supra-threshold perturbations. Once an supra-threshold perturbation excites a spike, the neuron is not able to respond to another perturbation before a given period of time called refractory time or period [39]. One method to extract the refractory period is to investigate the inter-spike time distribution induced by external noise sources [40, 41]. Such distribution is shown in Fig. 4g for $f_d - f_- = 0 \text{ kHz}$. As expected, when noise-induced transitions occur, the inter-spike time distributions follow an exponential decay given by a Kramer's type escape rate [42]. Interestingly, at short time scales, the inter-spike time distribution shows a pronounced dip, due to the impossibility to excite two response spikes that are arbitrarily close in time. This allows to extract the refractory period of the system which is of the order of $30 \mu s$.

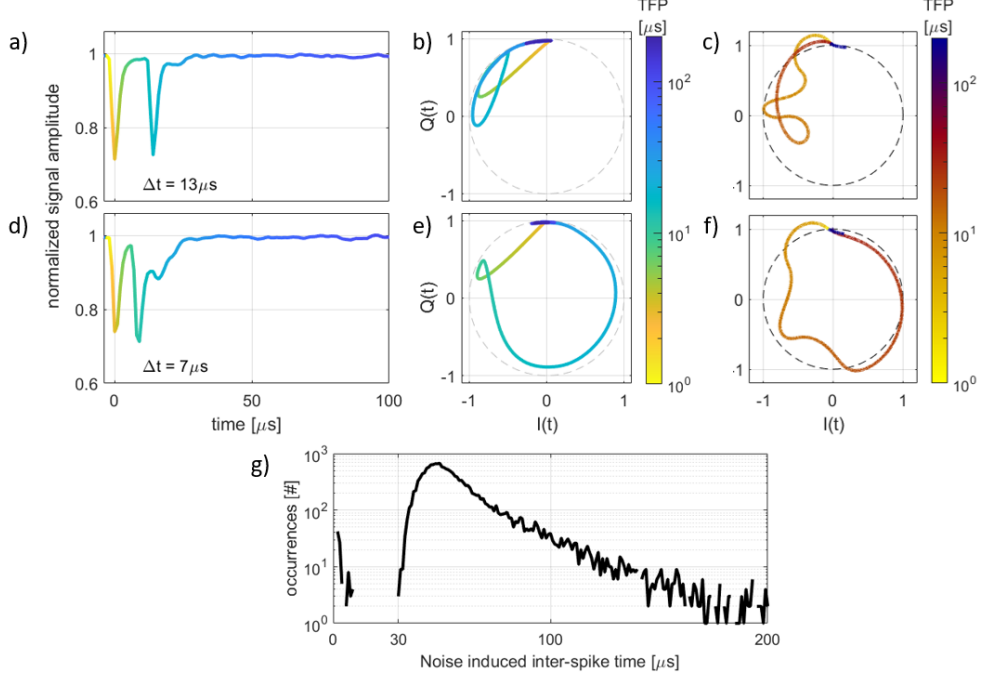


Figure 4 Temporal summation and refractory period dynamics. a,d) Experimental time traces and b,e) phase spaces in the cases of two sub-threshold perturbations separated by a time delay $\Delta t = 13 \mu s$ and $\Delta t = 7 \mu s$ respectively. c,f) Numerical simulations of the dynamics in the phase space with two sub-threshold perturbations arriving with time delays $\Delta t = 6 \mu s$ and $\Delta t = 4 \mu s$ respectively. g) Experimental distribution of the noise excited inter-spikes time for $f_d - f_- = 0$ kHz.

5 Conclusion

We have demonstrated an optomechanical spiking neuron based on silicon-integrated optical and electromechanical interfaces. The device operates at telecommunication wavelengths (1550 nm) and exploits a mechanical mode in the 3 GHz range, establishing a new nano-optomechanical platform for neuromorphic information processing.

This platform enables fully silicon-integrated, spike-based processing of optical and mechanical signals and is particularly well suited for edge-computing applications, where data processing is performed close to the signal source, thereby reducing latency

and bandwidth demands. Beyond signal processing, the device can provide an energy-efficient route to the generation of arbitrary on-chip optical spike sequences, offering a compact alternative to conventional Mach-Zehnder-based optical modulators, which typically require large footprints and high driving voltages.

The coexistence of optical and radio-frequency input ports enables a broad range of injection and control schemes that remain to be explored. These capabilities may enable on-chip cascability between multiple electro-optomechanical neurons, a key requirement for scalable neuromorphic architectures. Finally, the multiple optical and mechanical modes inherently supported by the nanobeam structure open opportunities for optical and mechanical multiplexing and parallel neuromorphic computing systems.

Acknowledgements. This work was funded by ANR project OptoMecaSNIC (ANR-24-CE24-3452) and PEPR Électronique - OROR (ANR-22-PEEL-0008). This work was partially supported by the French Renatech network.

6 Methods

Sample fabrication

A 300 nm thick gallium phosphide (GaP) layer with a 280 nm spacer layer of Silicon Nitride (SiN) is heterogeneously integrated on top of Silicon-on-Insulator (SoI) circuitry by wafer bonding. The optomechanical crystal as well as the surrounding pads are first patterned on GaP by electron beam lithography and dry-etching techniques. The 1 μm wide metallic electrodes are subsequently drawn on both sides of the crystal to ensure electromechanical excitation. Their relative position is chosen to be 1.5 μm away from the optical cavity to avoid degradation of its optical quality factor. Finally, dry-etching of the underlying SiN layer is performed allowing simultaneously a release of the optomechanical crystal and a fine control of the evanescent coupling between the SoI waveguide and the optical cavity.

Data acquisitions

The optical signal at the output of the integrated device is transduced into an electrical one by a 3.5 GHz bandwidth photo-detector. This signal is then mixed with the internal reference frequency f_d , and low-pass filtered with a demodulation bandwidth of 100 kHz. The data sampling rate of 1 MSa/s allows for the recording of a 1 s long time trace with a time resolution of 1 μ s inside which is recorded the E-OMO excitable response to 5000 equal input power perturbations.

Numerical model

The theoretical model consists of three coupled ODEs for the intracavity optical field $a(t)$, the mechanical mode displacement $x(t)$ and the nanobeam temperature elevation $\Delta T(t)$ and reads:

$$\begin{aligned}\dot{a}(t) &= \left[i \left(\Delta\omega + g_0 x(t) + \frac{\omega_L}{n_0} \kappa_{th} \Delta T \right) - \frac{\kappa}{2} \right] a(t) + \sqrt{\kappa_{ex}} s_{in}(t) \\ \ddot{x}(t) &= -\Gamma_m \dot{x}(t) - \Omega_m^2 x(t) + 2\Omega_m g_0 |a(t)|^2 + F_0 \sin(2\pi f_D t) \\ \dot{\Delta T}(t) &= \frac{\Gamma_{th}}{\tau_{th}} |a(t)|^2 - \frac{\Delta T(t)}{\tau_{th}}\end{aligned}$$

where $s_{in}(t) = \sqrt{\frac{P_{in}}{\hbar\omega_L} (1 + P_{pulse} S(2\pi f_P t, DC))}$ represents the input optical field. $P_{in} = 0.38$ mW is the input power in the bus waveguide to excite the OM self sustained oscillations, P_{pert} the perturbation pulse height with respect to P_{in} and $S(2\pi f_D t, DC)$ is the square wave signal with amplitude $\in [0, 1]$, frequency $f_P = 5$ kHz and duty-cycle DC. The optical mode amplitude $a(t)$ is driven by the input field $s_{in}(t)$ with a coupling constant κ_{ex} . The detuning between the input field and the cavity resonance is $\Delta\omega = \omega_L - \omega_{cav}$. The optomechanical coupling is $g_0 x(t)$ and the optical cavity is also subject to a thermally induced detuning where n_0 is the cavity material refractive index and κ_{th} the thermo-optic coefficient. The field decay

rate κ is calculated as $\kappa = \omega_{cav}/Q_o$ where Q_o is the optical resonance loaded quality factor. The mechanical displacement \tilde{x} is normalized to the zero-point-fluctuation displacement such that $x(t) = \tilde{x}(t)/x_{zpf}$, where $x_{zpf} = \sqrt{\hbar/2m_{eff}\Omega_m}$, with m_{eff} the mechanical oscillator effective mass and Ω_m its natural resonant frequency. The transmitted electric field intensity is calculated as $S_T(t) = |s_T(t)|^2 = |s_{in}(t) - \sqrt{\kappa_{ex}}a(t)|^2$.

The mechanical mode is described by the equation for a damped harmonic mechanical oscillator, that is driven by radiation pressure force and the piezoelectrical actuation $F_0 = F/m_{eff}x_{zpf}$, with F the driving force applied on the mechanical oscillator and f_D the driving frequency. $\Gamma_m = \Omega_m/Q_m$ where Q_m is the mechanical quality factor. The temperature increase of the cavity region $\Delta T(t)$ can be described by a source term which depends on the cavity absorption, and decays with a characteristic time τ_{th} , following [43]. The thermal load $\Gamma_{th} = R_{th}\hbar\omega_L\kappa_{abs}$ depends on the thermal resistance $R_{th} = \Delta x/k_{GaP}A$ with Δx the path parallel to the heat flow, k_{GaP} the thermal conductivity of gallium phosphide and A the cross section perpendicular to the heat flow. κ_{abs} is the decay rate due to photon absorptions in the cavity region, estimated as $\kappa_{abs} = 0.1\kappa_{in}$ [44].

The full parameters used for the numerical simulations are given in the Table 1 below.

Parameter	Value	Units	Comments	Ref.
λ_{cav}	1549	nm	cavity resonant wavelength	measure
$g_0/2\pi$	660	kHz	optomechanical coupling rate	measure
n_0	3.05	-	GaP refractive index @ $\lambda = 1550$ nm	[45]
$\kappa_{\Delta T}$	3.4×10^{-5}	K^{-1}	GaP TO coefficient	[46]
Q_o	40000	-	optical Quality factor	measure
κ	$2\pi c/\lambda_{cav} Q_O$	s^{-1}	cavity field decay rate	calc.
κ_{ex}	$\kappa/3$	s^{-1}	external decay rate	free param.
Q_m	1000	-	mechanical quality factor	measure
$\Omega_m/2\pi$	3078	MHz	mechanical frequency	measure
F	50	pN	external forcing	free param.
m_{eff}	10^{-16}	kg	effective mass	measure
Δx	40	μm	cavity length	design
k_{GaP}	110	W/mK	GaP thermal conductivity	[47]
A	300×700	nm^2	cavity cross section	design
τ_{th}	0.3	μs	thermal decay time const.	[48, 49]

Table 1 Table of values for electro-optomechanical equations

References

- [1] Marković, D., Mizrahi, A., Querlioz, D., Grollier, J.: Physics for neuromorphic computing. *Nat. Rev. Phys.* **2**(9), 499–510 (2020)
- [2] Maass, W.: Networks of spiking neurons: The third generation of neural network models. *Neural Networks* **10**(9), 1659–1671 (1997) [https://doi.org/10.1016/S0893-6080\(97\)00011-7](https://doi.org/10.1016/S0893-6080(97)00011-7)
- [3] Brunner, D., Shastri, B.J., Qadasi, M.A.A., Ballani, H., Barbay, S., Biasi, S., Bienstman, P., Bilodeau, S., Bogaerts, W., Böhm, F., Brennan, G., Buckley, S., Cai, X., Strinati, M.C., Canakci, B., Charbonnier, B., Chemnitz, M., Chen, Y., Cheung, S., Chiles, J., Choi, S., Christodoulides, D.N., Chrostowski, L., Chu, J., Clegg, J.H., Cletheroe, D., Conti, C., Dai, Q., Lauro, L.D., Diamantopoulos, N.P., Dinc, N.U., Ewaniuk, J., Fan, S., Fang, L., Franchi, R., Freire, P., Gentilini, S., Gigan, S., Giorgi, G.L., Gkantsidis, C., Gladrow, J., Goi, E., Goldmann, M., Grabulosa, A., Gu, M., Guo, X., Hejda, M., Horst, F., Hsieh, J.L., Hu, J., Hu, J., Huang, C., Hurtado, A., Jaurigue, L., Kalinin, K.P., Kopae, M.K., Kelly, D.J., Khajavikhan, M., Kremer, H., Laydevant, J., Lederman, J.C., Lee, J., Lenstra, D.,

Li, G.H.Y., Li, M., Li, Y., Lin, X., Lin, Z., Lis, M., Lüdge, K., Lugnan, A., Lupo, A., Lvovsky, A.I., Manuylovich, E., Marandi, A., Marchesin, F., Massar, S., McCaughan, A.N., McMahon, P.L., Pegios, M.M., Morandotti, R., Moser, C., Moss, D.J., Mukherjee, A., Nikdast, M., Offrein, B.J., Oguz, I., Oripov, B., O'Shea, G., Ozcan, A., Parmigiani, F., Pasricha, S., Pavanello, F., Pavesi, L., Peserico, N., Pickup, L., Pierangeli, D., Pleros, N., Porte, X., Primavera, B.A., Prucnal, P., Psaltis, D., Puts, L., Qiao, F., Rahmani, B., Rainieri, F., Ocampo, C.A.R., Robertson, J., Romeira, B., Carmes, C.R., Rotenberg, N., Rowstron, A., Schoenhardt, S., Schwartz, R.L..T., Shainline, J.M., Shekhar, S., Skalli, A., Sohoni, M.M., Sorger, V.J., Soriano, M.C., Spall, J., Stabile, R., Stiller, B., Sunada, S., Tefas, A., Tossoun, B., Tsakyridis, A., Turitsyn, S.K., Sande, G.V., Vaerenbergh, T.V., Veraldi, D., Verschaffelt, G., Vlieg, E.A., Wang, H., Wang, T., Wetzstein, G., Wright, L.G., Wu, C., Wu, C., Wu, J., Xia, F., Xu, X., Yang, H., Yao, W., Yildirim, M., Yoo, S.J.B., Youngblood, N., Zambrini, R., Zhang, H., Zhang, W.: Roadmap on Neuromorphic Photonics (2025). <https://arxiv.org/abs/2501.07917>

- [4] Chou, C.-N., Chung, K.-M., Lu, C.-J.: On the Algorithmic Power of Spiking Neural Networks. In: Blum, A. (ed.) 10th Innovations in Theoretical Computer Science Conference (ITCS 2019). Leibniz International Proceedings in Informatics (LIPIcs), vol. 124, pp. 26–12620. Schloss Dagstuhl – Leibniz-Zentrum für Informatik, Dagstuhl, Germany (2019). <https://doi.org/10.4230/LIPIcs.ITCS.2019.26> . <https://drops.dagstuhl.de/entities/document/10.4230/LIPIcs.ITCS.2019.26>
- [5] Verzi, S.J., Rothganger, F., Parekh, O.D., Quach, T.-T., Miner, N.E., Vineyard, C.M., James, C.D., Aimone, J.B.: Computing with spikes: The advantage of fine-grained timing. Neural Computation **30**(10), 2660–2690 (2018) https://doi.org/10.1162/neco_a_01113 https://direct.mit.edu/neco/article-pdf/30/10/2660/1046612/neco_a_01113.pdf

[6] Feldmann, J., Youngblood, N., Karpov, M., Gehring, H., Li, X., Stappers, M., Le Gallo, M., Fu, X., Lukashchuk, A., Raja, A.S., Liu, J., Wright, C.D., Sebastian, A., Kippenberg, T.J., Pernice, W.H.P., Bhaskaran, H.: Parallel convolutional processing using an integrated photonic tensor core. *Nature* **589**, 52–58 (2021) <https://doi.org/10.1038/s41586-020-03070-1>

[7] Gautrais, J., Thorpe, S.: Rate coding versus temporal order coding: a theoretical approach. *Biosystems* **48**(1), 57–65 (1998) [https://doi.org/10.1016/S0303-2647\(98\)00050-1](https://doi.org/10.1016/S0303-2647(98)00050-1)

[8] Stöckl, C., Maass, W.: Optimized spiking neurons can classify images with high accuracy through temporal coding with two spikes. *Nat. Mach. Intell.* **3**(3), 230–238 (2021)

[9] Göltz, J., Kriener, L., Baumbach, A., Billaudelle, S., Breitwieser, O., Cramer, B., Dold, D., Kungl, A.F., Senn, W., Schemmel, J., Meier, K., Petrovici, M.A.: Fast and energy-efficient neuromorphic deep learning with first-spike times. *Nat. Mach. Intell.* **3**(9), 823–835 (2021)

[10] Rao, A., Plank, P., Wild, A., Maass, W.: A long short-term memory for AI applications in spike-based neuromorphic hardware. *Nat. Mach. Intell.* **4**(5), 467–479 (2022)

[11] Thomas, A.: Memristor-based neural networks. *Journal of Physics D: Applied Physics* **46**(9), 093001 (2013) <https://doi.org/10.1088/0022-3727/46/9/093001>

[12] Marković, D., Daniels, M.W., Sethi, P., Kent, A.D., Stiles, M.D., Grollier, J.: Easy-plane spin hall nano-oscillators as spiking neurons for neuromorphic computing. *Phys. Rev. B* **105**, 014411 (2022) <https://doi.org/10.1103/PhysRevB.105.014411>

[13] Mishra, A., Ghosh, S., Kumar Dana, S., Kapitaniak, T., Hens, C.: Neuron-like spiking and bursting in josephson junctions: A review. *Chaos: An Interdisciplinary Journal of Nonlinear Science* **31**(5), 052101 (2021) <https://doi.org/10.1063/5.0050526> https://pubs.aip.org/aip/cha/article-pdf/doi/10.1063/5.0050526/19773926/052101_1_online.pdf

[14] Pedaci, F., Huang, Z., Oene, M., Barland, S., Dekker, N.H.: Excitable particles in an optical torque wrench. *Nat. Phys.* **7**(3), 259–264 (2011)

[15] Plaza, F., Velarde, M.G., Arecchi, F.T., Boccaletti, S., Ciofini, M., Meucci, R.: Excitability following an avalanche-collapse process. *EPL* **38**(2), 85–90 (1997)

[16] Giudici, M., Green, C., Giacomelli, G., Nespolo, U., Tredicce, J.R.: Andronov bifurcation and excitability in semiconductor lasers with optical feedback. *Phys. Rev. E* **55**(6), 6414–6418 (1997)

[17] Wünsche, H.J., Brox, O., Radziunas, M., Henneberger, F.: Excitability of a semiconductor laser by a two-mode homoclinic bifurcation. *Phys. Rev. Lett.* **88**(2), 023901 (2002)

[18] Barland, S., Piro, O., Giudici, M., Tredicce, J.R., Balle, S.: Experimental evidence of van der Pol-Fitzhugh-Nagumo dynamics in semiconductor optical amplifiers. *Phys. Rev. E* **68**(3 Pt 2), 036209 (2003)

[19] Goulding, D., Hegarty, S.P., Rasskazov, O., Melnik, S., Hartnett, M., Greene, G., McInerney, J.G., Rachinskii, D., Huyet, G.: Excitability in a quantum dot semiconductor laser with optical injection. *Phys. Rev. Lett.* **98**(15), 153903 (2007)

[20] Beri, S., Mashall, L., Gelens, L., Sande, G., Mezosi, G., Sorel, M., Danckaert, J., Verschaffelt, G.: Excitability in optical systems close to -symmetry. *Phys. Lett.*

- [21] Barbay, S., Kuszelewicz, R., Yacomotti, A.M.: Excitability in a semiconductor laser with saturable absorber. *Opt. Lett.* **36**(23), 4476–4478 (2011) <https://doi.org/10.1364/OL.36.004476>
- [22] Izhikevich, E.M.: *Dynamical Systems in Neuroscience: The Geometry of Excitability and Bursting*. The MIT Press, ??? (2006). <https://doi.org/10.7551/mitpress/2526.001.0001> . <https://doi.org/10.7551/mitpress/2526.001.0001>
- [23] Rohlev, A., Radehaus, C., Pankove, J.I., Carson, R.F., Borglis, G.: Optoelectronic neuron. In: *Optical Computing*, p. 5. Optica Publishing Group, ??? (1991). <https://doi.org/10.1364/OPTCOMP.1991.ME5> . <https://opg.optica.org/abstract.cfm?URI=OPTCOMP-1991-ME5>
- [24] Romeira, B., Javaloyes, J., Ironside, C.N., Figueiredo, J.M.L., Balle, S., Piro, O.: Excitability and optical pulse generation in semiconductor lasers driven by resonant tunneling diode photo-detectors. *Opt. Express* **21**(18), 20931–20940 (2013) <https://doi.org/10.1364/OE.21.020931>
- [25] Chen, J., Zhou, Z., Kim, B.J., Zhou, Y., Wang, Z., Wan, T., Yan, J., Kang, J., Ahn, J.-H., Chai, Y.: Optoelectronic graded neurons for bioinspired in-sensor motion perception. *Nature Nanotechnology* **18**, 882 (2023) <https://doi.org/10.1038/s41565-023-01379-2>
- [26] Li, H., Hu, J., Zhang, Y., Chen, A., Zhou, J., Zhao, Y., Xu, Y., Yu, B.: Single-transistor optoelectronic spiking neuron with optogenetics-inspired spatiotemporal dynamics. *Advanced Functional Materials* **34**(22), 2314456 (2024) <https://doi.org/10.1002/adfm.202314456> <https://advanced.onlinelibrary.wiley.com/doi/pdf/10.1002/adfm.202314456>

[27] Guo, X., Yang, W., Xiong, X., Wang, Z., Zou, X.: Mems reservoir computing system with stiffness modulation for multi-scene data processing at the edge. *Microsystems & Nanoengineering* **10**(1), 84 (2024) <https://doi.org/10.1038/s41378-024-00701-9>

[28] Dion, G., Oudrhiri, A.I.-E., Barazani, B., Tessier-Poirier, A., Sylvestre, J.: In: Nakajima, K., Fischer, I. (eds.) *Reservoir Computing in MEMS*, pp. 191–217. Springer, Singapore (2021). https://doi.org/10.1007/978-981-13-1687-6_9 . https://doi.org/10.1007/978-981-13-1687-6_9

[29] Jin, L., Liu, Z., Li, L.: A novel reservoir computing platform constructed by laser controlled gaas resonator. *IEEE Electron Device Letters* **43**(9), 1563–1566 (2022) <https://doi.org/10.1109/LED.2022.3194577>

[30] Dion, G., Mejaouri, S., Sylvestre, J.: Reservoir computing with a single delay-coupled non-linear mechanical oscillator. *Journal of Applied Physics* **124**(15), 152132 (2018) <https://doi.org/10.1063/1.5038038> https://pubs.aip.org/aip/jap/article-pdf/doi/10.1063/1.5038038/19764747/152132_1_online.pdf

[31] Yang, Y., Deng, Y., Xiong, X., Shi, B., Ge, L., Wu, J.: Neuron-like optical spiking generation based on silicon microcavity. In: 2020 IEEE 20th International Conference on Communication Technology (ICCT), pp. 970–974 (2020). <https://doi.org/10.1109/ICCT50939.2020.9295847>

[32] Aspelmeyer, M., Kippenberg, T.J., Marquardt, F.: Cavity optomechanics. *Rev. Mod. Phys.* **86**, 1391–1452 (2014) <https://doi.org/10.1103/RevModPhys.86.1391>

[33] Barzanjeh, S., Xuereb, A., Gröblacher, S., Paternostro, M., Regal, C.A., Weig, E.M.: Optomechanics for quantum technologies. *Nature Physics* **18**, 15–24 (2022)

<https://doi.org/10.1038/s41567-021-01402-0>

- [34] Horváth, R., Modica, G., Ghorbel, I., Beaudoin, G., Pantzas, K., Sagnes, I., Martin, A., De Rossi, A., Combrié, S., Braive, R.: Sub-hz closed-loop electro-optomechanical oscillator with gallium phosphide photonic crystal integrated on soi circuitry. *ACS Photonics* **10**(8), 2540–2548 (2023) <https://doi.org/10.1021/acsphtnics.3c00074> <https://doi.org/10.1021/acsphtnics.3c00074>. PMID: 37602296
- [35] Jiang, W.C., Lin, Q.: Chip-scale cavity optomechanics in lithium niobate. *Scientific Reports* **6**(1), 36920 (2016)
- [36] Bekker, C., Kalra, R., Baker, C., Bowen, W.P.: Injection locking of an electro-optomechanical device. *Optica* **4**(10), 1196–1204 (2017) <https://doi.org/10.1364/OPTICA.4.001196>
- [37] Masominia, A., Calvet, L.E., Thorpe, S., Barbay, S.: Online spike-based recognition of digits with ultrafast microlaser neurons. *Frontiers in Computational Neuroscience* **Volume 17 - 2023** (2023) <https://doi.org/10.3389/fncom.2023.1164472>
- [38] Selmi, F., Braive, R., Beaudoin, G., Sagnes, I., Kuszelewicz, R., Barbay, S.: Temporal summation in a neuromimetic micropillar laser. *Opt. Lett.* **40**(23), 5690–5693 (2015) <https://doi.org/10.1364/OL.40.005690>
- [39] Purves, D. (ed.): *Neuroscience*, Sixth edition edn. Oxford University Press, New York (2018)
- [40] Eguia, M.C., Mindlin, G.B.: Distribution of interspike times in noise-driven excitable systems. *Phys. Rev. E* **61**, 6490–6499 (2000) <https://doi.org/10.1103/PhysRevE.61.6490>

[41] Pedaci, F., Huang, Z., Oene, M., Barland, S., Dekker, N.H.: Excitable particles in an optical torque wrench. *Nature Physics* **7**, 259 (2011) <https://doi.org/10.1038/nphys1862>

[42] Kramers, H.A.: Brownian motion in a field of force and the diffusion model of chemical reactions. *Physica* **7**(4), 284–304 (1940) [https://doi.org/10.1016/S0031-8914\(40\)90098-2](https://doi.org/10.1016/S0031-8914(40)90098-2)

[43] Guha, B., Mariani, S., Lemaître, A., Combrié, S., Leo, G., Favero, I.: High frequency optomechanical disk resonators in III-V ternary semiconductors. *Optics Express* **25**(20), 24639 (2017) <https://doi.org/10.1364/OE.25.024639> . arXiv:1710.00632 [physics]. Accessed 2025-07-02

[44] Zhang, L., Fei, Y., Cao, T., Cao, Y., Xu, Q., Chen, S.: Multibistability and self-pulsation in nonlinear high- Q silicon microring resonators considering thermo-optical effect. *Physical Review A* **87**(5), 053805 (2013) <https://doi.org/10.1103/PhysRevA.87.053805> . Accessed 2024-07-29

[45] Tian, H., Liu, J., Attanasio, A., Siddharth, A., Blésin, T., Wang, R.N., Voloshin, A., Lihachev, G., Riemensberger, J., Kenning, S.E., Tian, Y., Chang, T.H., Bancora, A., Snigirev, V., Shadymov, V., Kippenberg, T.J., Bhave, S.A.: Piezoelectric actuation for integrated photonics. *Advances in Optics and Photonics* **16**(4), 749–867 (2024) <https://doi.org/10.1364/AOP.529288> . Publisher: Optica Publishing Group. Accessed 2025-05-12

[46] Lake, D.P., Mitchell, M., Jayakumar, H., Santos, L.F., Curic, D., Barclay, P.E.: Efficient telecom to visible wavelength conversion in doubly resonant gallium phosphide microdisks. *Applied Physics Letters* **108**(3), 031109 (2016) <https://doi.org/10.1063/1.4940242> . Accessed 2025-09-08

[47] Levenshtein, M., Shur, M.: Handbook Series on Semiconductor Parameters: Ternary and Quaternary III-V compounds. World Scientific, ??? (1999). Google-Books-ID: zLvACwAAQBAJ

[48] Chan, J., Safavi-Naeini, A.H., Hill, J.T., Meenehan, S., Painter, O.: Optimized optomechanical crystal cavity with acoustic radiation shield. *Applied Physics Letters* **101**(8), 081115 (2012) <https://doi.org/10.1063/1.4747726> . Accessed 2025-08-12

[49] Navarro-Urrios, D., Capuj, N.E., Gomis-Bresco, J., Alzina, F., Pitanti, A., Griol, A., Martínez, A., Sotomayor Torres, C.M.: A self-stabilized coherent phonon source driven by optical forces. *Scientific Reports* **5**(1), 15733 (2015) <https://doi.org/10.1038/srep15733> . Accessed 2024-07-29